ELSEVIER

Materials Science and Engineering A 418 (2006) 341–356

MATERIALS SCIENCE & ENGINEERING A

www.elsevier.com/locate/msea

Microstructural effects of AZ31 magnesium alloy on its tensile deformation and failure behaviors

Manuel Marya [a,*,1], Louis G. Hector [b], Ravi Verma [b], Wei Tong [c]

[a] *Colorado School of Mines, Metallurgical and Materials Engineering Department, Center for Welding, Joining & Coatings Research, 1500 Illinois Street, Golden, CO 80401, United States*

[b] *General Motors R&D Center, 30500 Mound Road, Warren, MI 48090, United States*

[c] *Southern Methodist University, 6001 Dublin Street, Dallas, TX 75275-0337, United States*

Accepted 3 December 2005

Abstract

An Mg AZ31 alloy with modified microstructures was investigated to determine microstructural effects on room temperature mechanical properties acquired from low strain rate ($\sim 10^{-3}\ s^{-1}$) tensile testing to failure. Three distinct microstructures were generated via heat treatment, viz.: (1) single phase, fine equiaxed grains; (2) single phase, coarse grains with twins; (3) fine, equiaxed grains decorated with $Mg_{17}(Al,Zn)_{12}$ grain-boundary precipitates. Each microstructure was separately characterized with optical microscopy, X-ray crystallography, fractography, and hardness measurement prior to tensile testing. Tensile coupons fabricated from each microstructure were then elongated to failure in a miniature stage, and true stress–true strain curves were computed with the digital image correlation (DIC) technique. Initial yield point, ultimate tensile strength and maximum elongation were also computed and examined within the context of key features of each microstructure to infer the mechanism of plastic deformation in tension and whether or not the potential for improved room temperature formability exists.

Keywords: Tension test; Image correlation strain mapping; Mg alloy; Ductile failure

1. Introduction

Magnesium alloys exhibit the attractive combination of low densities (1.74 g/cm^3 versus 2.7 g/cm^3 for Al) and high strength per weight ratios (comparable or greater than that of precipitation strengthened Al alloys), along with good damping capacity, castability, weldability, and machinability [1,2]. Of the various commercial Mg alloys, those developed from the Al–Zn ternary system (i.e. the as-named AZ alloys) have found the largest number of industrial applications. Major commercial grades of AZ alloys are AZ31, AZ61 and AZ91, which are produced either as cast products (e.g. die, sand and mold castings) or wrought products (e.g. extrusions, forgings, sheet and plates). In general, as Al content of the alloy increases, yield strength, ultimate tensile strength, corrosion resistance and oxidation resistance all increase, whereas castability and weldability rapidly decrease. The formation of stable solid solutions and second phases with increasing Al content raise the yield point of sand-cast AZ alloys from 50 MPa in AZ31 to 93 MPa in AZ91 (for example) [3]. The effect of Al on ductility, or maximum elongation during tensile testing, is less predictable since Al is capable of either increasing or decreasing mechanical strength depending upon heat-treatments [4]. In general, significant amounts of Al, Zn and/or Mn reduce ductility due to the formation of brittle second phases. Compared to Al, Zn is more effective in increasing strength as a substitutional solid solution element and reducing ductility. The Al contribution to corrosion resistance, or oxidation resistance, is beneficial. Most importantly, Al promotes the formation of passive and resistant complex Al oxide/hydroxide layers at the surface of Mg [5]: the formation of such films is a major contributing factor to the reduction of Mg reactivity in dry or moist environments. In addition to Al, other alloying elements, such as Ca, Sc, Y, and Zr, have been investigated for their potential impact on Mg alloy mechanical properties [6]. Of the few AZ commercial alloys, the AZ31 alloy represents a good compromise between strength, ductility, and cost, and is probably the best choice for stamping operations. At the present time, AZ91 is the most commonly used AZ alloy in the automotive industry.

* Corresponding author. Present address: Schlumberger, 14910 Airline Road, Rosharon, TX 77581, USA

E-mail address: mmarya@rosharon.oilfield.slb.com (M. Marya).

[1] On assignment at General Motors R&D Center.

0921-5093/$ – see front matter © 2005 Elsevier B.V. All rights reserved.
doi:10.1016/j.msea.2005.12.003

Compared to conventional steel sheets used in vehicle structures, Mg alloys have poor ductility and fracture toughness at ambient temperature [1,2,7]. In contrast to the high ductility of the cubic lattice of ferrous alloys, the low ductility of Mg alloys is often explained by a lack of slip systems inherent to its hexagonal-close packed (HCP) lattice. Moreover, the nearly ideal *c*/*a* ratio promotes twinning, rather than basal or prismatic slip [1,8]. Twinning is an athermal shear deformation process involving mirrored movement of several unbroken atomic layers, which, unlike dislocation slip where atomic bonds are broken, considerably reduces ductility [9]. While conventional stamping of Mg alloys is problematic, high-temperature forming facilitates the manufacture of near-net shapes from Mg alloy sheets. In recent years, high-temperature forming of Mg alloys has received significant attention. In fact, complex shapes have been fabricated from AZ31 sheets, as reported by several investigators [10–12]. Magnesium alloys based on Li are currently of interest due to the formation of body-centered cubic lithium phases with large numbers of dislocation slip systems and therefore high room-temperature formability [13–15]. Although such alloys offer important benefits for forming (e.g. stamping, hydroforming, etc.), immediate application for Mg sheet products is likely to begin with readily available grades, and in this respect AZ31 is in excellent position for wider use in automotive body applications.

In this article, the properties of wrought AZ31 sheets in the O-temper state, typically obtained after hot blow forming (e.g. quick plastic forming [16]) are investigated. Specifically, AZ31 microstructures were produced with: (1) a single-phase fine equiaxed grain structure; (2) a single-phase coarse grain structure; (3) a fine equiaxed grain structure decorated with fine $Mg_{17}(Al,Zn)_{12}$ intermetallic particles. The effects of microstructure, in particular grain size and second-phase precipitates formed by aging of the supersaturated solid solution, on mechanical properties, particularly tensile stress–strain behavior and hardness (via indentation), were investigated to determine which microstructure might offer the best ambient temperature formability. The digital image correlation (DIC) technique was used to measure tensile true stress–strain curves up to the point of localized necking using a miniature tensile stage and a custom image acquisition system. Fracture surfaces of each microstructure were examined via SEM. This provided a basis for comparison of the tensile deformation and fracture behavior of the three microstructures.

The remainder of this paper is organized as follows. In Section 2, the experimental components of the work, which included preparation of the Mg microstructures and mechanical testing methodologies (microhardness measurement, tensile testing, and analysis of plastic deformation via digital image correlation), are detailed. In Section 3, the results of the experiments are described. These include Mg microstructural characterization, raw force–displacement curves and true stress–true strain relations, contours of the in-plane strain fields derived from DIC, and fracture surface analysis. In Section 4, the major results from the work are summarized and suggestions for future investigations of Mg alloys are offered.

Table 1
Chemical composition (wt.%) of the AZ31 material of this study

Al	2.34–2.37
Zn	1.04–1.11
Mn	0.12–0.14
Si	0.06–0.11
Mg	Balance

2. Experimental procedure

2.1. Materials

Nominal composition of the as-received (hot rolled) AZ31 sheet, as measured by wavelength dispersive spectroscopy, is given in Table 1. The as-received sheet was cut into rectangular coupons that were heat-treated to produce the desired three microstructures.

A first set of coupons was prepared with single phase, fine recrystallized grains, obtained after a solution heat-treatment at 450 °C for 1 min (quenched in room temperature water). The resulting microstructure (1) is referred to as the "base" microstructure. A second set of samples was generated by prolonging the solution heat-treatment (SHT) to about 10 min: this microstructure (2) is referred to as the 10-min SHT microstructure. During this additional time, the growth of recrystallized grains from the first heat-treatment was stimulated. A temperature of 450 °C was selected based upon the binary Mg–Al equilibrium phase diagram [17]. This is nearly the Mg–Al eutectic temperature on the Mg-rich side of the binary phase diagram, and solid-solubility of Al in the α-Mg phase is maximal (approximately 12 wt.%). Note that cooling in air followed both solution heat-treatments. A third set of coupons was prepared from the first (i.e. base) set, simply by adding a low-temperature aging heat-treatment of 3 days at 160 °C: this microstructure (3) is referred to as the (3-day) aged microstructure. The 160 °C temperature was also selected from the Mg–Al equilibrium phase diagram since a significant amount of the $Mg_{17}(Al,Zn)_{12}$ phase is in thermodynamic equilibrium with α-Mg. Hence, the third microstructure was produced with the intention of precipitating a fine dispersion of the second phase ($Mg_{17}(Al,Zn)_{12}$) in the matrix phase. Since grain boundaries and internal defects act as heterogeneous nucleation sites for diffusional phase growth, the microstructure (1) with fine grains (i.e. the base alloy, as it now referred to) was preferred for the aging heat-treatment. The 3-day aging period was arbitrarily selected with the hope that it would be sufficient for $Mg_{17}(Al,Zn)_{12}$ to fully precipitate to its equilibrium concentration along grain boundaries and other internal defects.

Samples of each of the three microstructures were prepared using standard metallographic techniques. A solution of 50-ml picric acid, 20-ml glacial acetic acid, 10-ml deionized water, and 10-ml methanol was prepared as an etchant and briefly applied to the polished surface of each sample, which was then thoroughly rinsed with deionized water and ethanol. Both optical microscopy and scanning electron microscopy were used to examine the microstructural details. The SEM electron beam

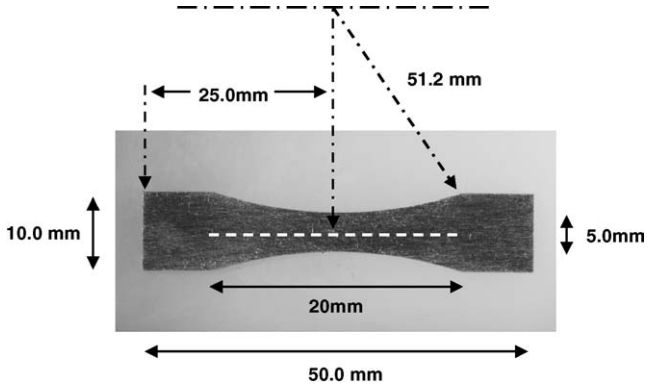

Fig. 1. Magnesium tensile coupon with 2.0 mm thickness.

accelerating voltage was set between 5 and 13 kV, depending upon desired magnification or the need for chemical analysis by energy dispersive spectroscopy. Chemical compositions at the surfaces of unetched samples were measured using wavelength dispersive spectrometers from a microprobe microanalyzer. X-ray diffraction was used to identify the phases and to explore solute depletion of the α-Mg phase as a possible consequence of the aging treatment.

2.2. Tensile coupon geometry and indentation measurement

All three heat-treated microstructures were micro-indented under 100 mN to explore differences in the microhardness. Indentation scans were repeated at least six times at random starting locations to calculate average Vickers microhardness.

Small tensile coupons were fabricated from each of the three Mg microstructures using electrical-discharge machining (EDM). Fig. 1 shows the as-machined tensile coupon geometry. The 2 mm-thick tensile coupons were 50.0 mm in overall length with a 10.0 mm gripper width. Two arcs, with a 51.2 mm radius, formed the opposite sides of a 20 mm-long gauge section, as shown. The curved gauge section geometry ensured that localization and failure occurred at the gauge section center, which had a minimum width of 5 mm. This facilitated digital image acquisition during the tensile tests without adversely influencing the subsequent measurement of two-dimensional (2D) deformation fields in the gauge section. As shown in Fig. 2, which is a 607 μm × 462 μm white light interference microscope image of an Mg tensile coupon surface topography, the EDM surface roughness was well within acceptable limits for tensile testing (R_a = 3.81 μm). Surfaces produced with EDM are notable for their "cratered" appearance that results from the expulsion of liquid metal rims (light regions) that overlap one-another due to spark movement.

Prior to testing, one surface of each Mg tensile coupon was decorated with a high density of unique contrast features. What was found to work best for the DIC analysis was a dense coating of white spray paint droplets, followed by a less dense coating of black spray paint droplets. Several initial tests of one paint color or the other proved inadequate for the image correlation process.

2.3. Digital image correlation and instrumentation

Two-dimensional digital image correlation (DIC) is a fast and precise method for measuring in-plane deformation and displacement fields of plastically deforming sheet metals. The input to the correlation algorithm requires a set of digital images that store the deformation history recorded from one surface of the deforming metal up to fracture. Once a test is completed, the images can then be compared in a cumulative fashion, in which an earlier image is compared with a later image, or in an incremental fashion, in which temporally successive image pairs are compared to produce deformation and displacement history. Prior applications of the DIC technique of relevance to the present study involved stress–strain characterization (up to fracture) of miniature dual-phase steel spot welds [18], and measurement of Portevin–LeChatlier band propagation during tensile deformation of an Al–Mg alloy with a high speed digital camera [19]. The digital image correlation analyses of all test results were conducted with the SDMAP3D program developed by Tong et al. [20–23].

Digital images (in bitmap format) of one surface of each tensile coupon were recorded at a maximum rate of 2-s inter-

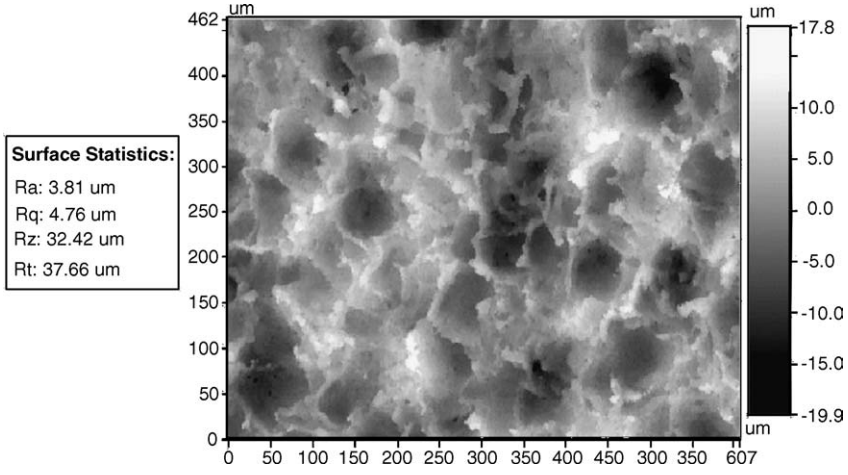

Fig. 2. Optical interference microscope image of EDM surface on Mg tensile coupon.

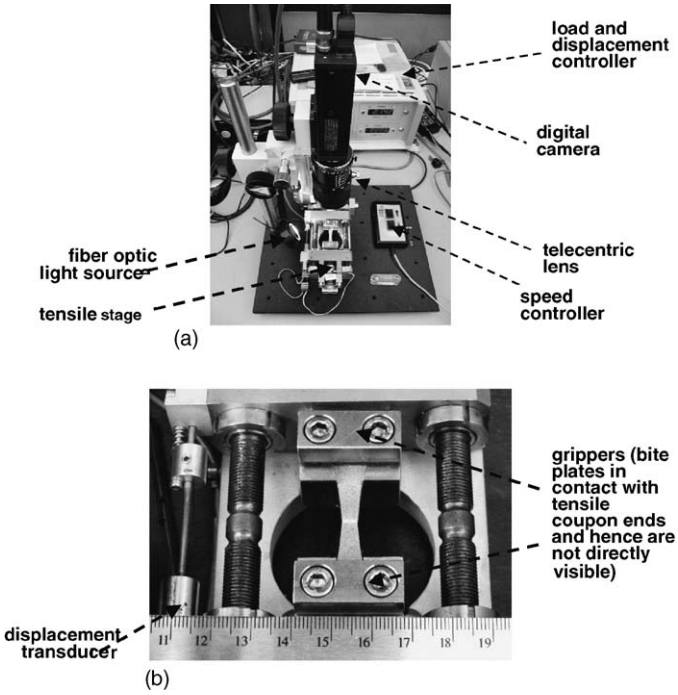

Fig. 3. (a) Monochrome digital camera with telecentric lens focused on Mg tensile coupon. Tensile stage with load cell (front), controller (white box with digital display in background), and speed controller (mouse with two buttons to the right of the tensile stage) is also shown. Light diffusing curtain is not shown. (b) Tensile stage with Mg tensile coupon moments after fracture. Note the displacement transducer on the left side of the stage.

vals throughout each tensile test using a digital camera (SONY monochrome model XCD-SX900). The camera was aligned along a vertical axis directly above the tensile coupon surface at a distance of 40 cm. This experimental configuration is shown in Fig. 3a. A telecentric lens, which eliminated magnification-induced distortions across the field of view of the camera, was used to image the tensile coupon surface loaded in the tensile stage (also shown in Fig. 3a). Lens adjustments enabled capture of either the entire gauge section or a portion of the gauge section near its center (for example) where localization and fracture were anticipated. The surface of each tensile coupon was illuminated with light from a diffuse fiber-optic light source. Image intensity and depth of field were controlled with the lens f-stop (adjusted to allow the desired amount of light into the camera), and the image exposure time (typically 1/32 s) was adjusted through the image acquisition software. The pixel density of each recorded image was set to the native 1280×960 pixels resolution of the camera, which had a framing rate of 7 frames/s.

Digital images captured with the camera/lens assembly were triggered with a custom time and force-based image acquisition algorithm that was engineered with the DASYLab data acquisition and test control programming software [24]. The software triggered the digital camera at either 10 s intervals, or if the force fluctuations exceeded +10% or −2% during sampling of the load. Once an image was captured by the camera, it was saved with an image capturing software program (written in C++) which gave the image a sequential file name and then saved it in bitmap format. When all of the images for a given test were acquired, the DASYLAb program commanded an Excel-Visual Basic program to create a folder on the DASYLab PC (the image acquisition and storage process involved two PCs) with the name of the test and a time stamp, and then moved the files from the image capture PC to the newly created folder on the DASYLab PC. The Visual-Basic program then created a separate file that correlated all of the bitmap images files with the test specimen name, load and displacement corresponding to each image. What resulted from this process was an additional set of the same bitmap images recorded during the test, but with file names that could be readily input to the SDMAP DIC software program.

The tensile stage was manufactured by Kammrath–Weiss in Dortmund, Germany [25], and had a 20 mm displacement range and a 5 kN load cell. One revolution of the screws produces 2 μm of crosshead displacement. All Mg tensile coupons were strained to fracture at a constant crosshead speed of 1.8×10^{-2} mm/s. Note that the crosshead speed was controlled through the 2.0×10^{-3} to 2.0×10^{-2} mm/s range via the hand-held speed controller shown in Fig. 3a. Special stainless steel grippers (see Fig. 3b) with hardened steel bite plates having serrated surfaces were manufactured to accommodate the gripper ends of the tensile coupon in Fig. 1, and to prevent slippage of the gripped ends during testing. Load values were recorded from the tensile stage and displacement controller (see Fig. 3a) via an RS232 connection at a 3 Hz rate. An enlarged view of the tensile stage and displacement transducer is shown in Fig. 3b following fracture of an Mg tensile coupon.

Examples of raw data recorded during the tests are displayed in Fig. 4. Fig. 4a shows that between transient periods associated with the start of the test and complete fracture (i.e. termination of the test), the average loading speed was 1.8×10^{-2} mm/s. This signal typically contains some noise from the acquisition electronics. Fig. 4b shows that the crosshead displacement was linear with time following an initial startup delay. The crosshead load or force increased linearly with time, as shown in Fig. 4c, up to the point of yielding around 2700 N. The measured strain rate change with time, depicted in Fig. 4d, shows that the strain rate increased with time but at a very slow rate. The nominal strain rate in the tensile coupon reached to a level of 8.0×10^{-4} s^{-1} and higher. Fig. 4e shows that a maximum average strain of 0.10 mm/mm was achieved at $t = 125$ s. Finally, Fig. 4f shows the engineering stress variation with time. Note that a peak stress of 300 MPa was achieved around 75 s into the test.

Once testing was completed, the DIC algorithm was directed to compute 2D displacement and strain fields by tracking changes in the position and orientation of the unique contrast features from image to image. A digital grid pattern was computed and superimposed onto each image pair used in the correlation process. The grid pattern, which serves as a digital strain gauge that follows the curved geometry of the gauge section of each tensile coupon surface, consisted of 76 points along the X_1 direction (see Fig. 5a) and 25 points in the X_2 direction. The 1900-point grid pattern was found to adequately resolve displacements and strains computed from the tensile coupon surface via the DIC algorithm. Examples of grid patterns on an Mg tensile surface prior to tensile testing, and just before the

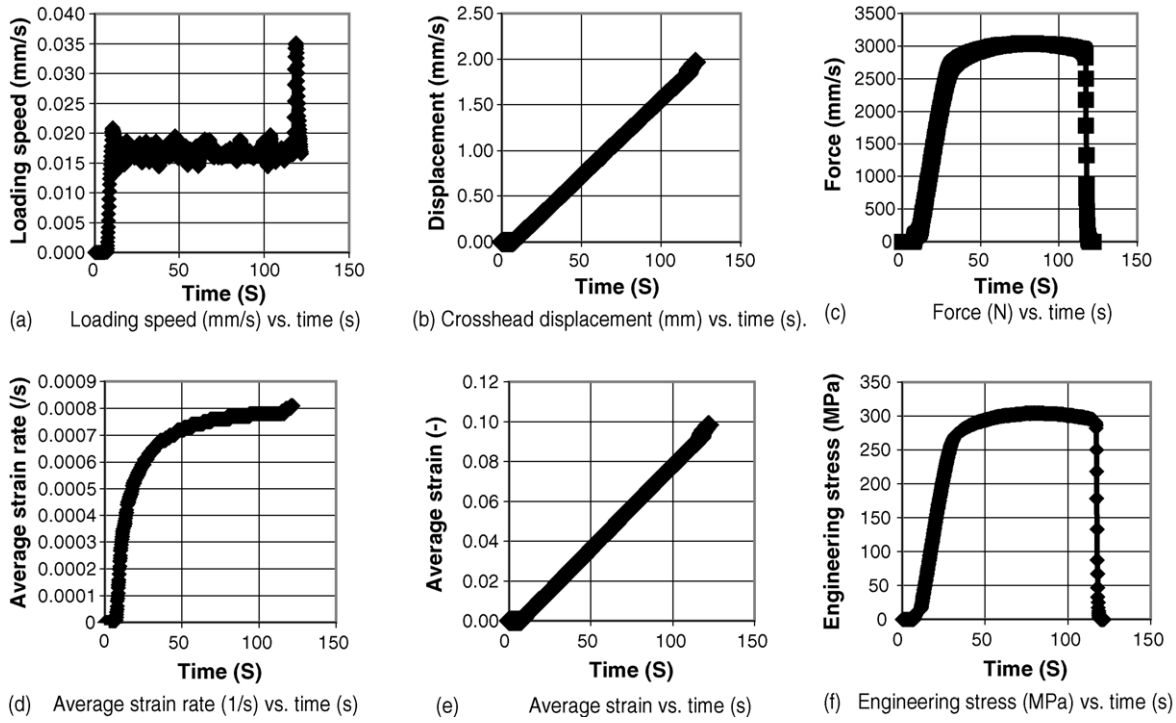

Fig. 4. Representative raw data recorded with DASYLab [24] acquisition program during tensile testing of Mg coupons.

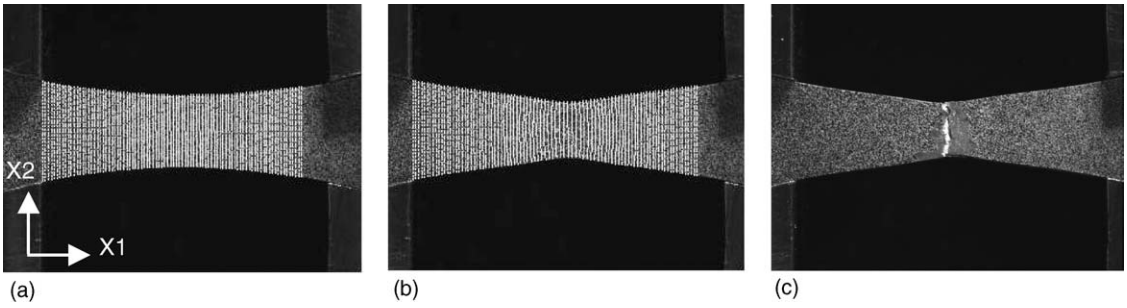

Fig. 5. Digital images of Mg tensile coupon before testing (a), toward the end of the test (b), and after fracture (c). Blue grid pattern which defines the points at which the strains and displacements are computed in the correlation process are shown in (a) and (b). Note the contrast pattern, which is especially obvious in (c).

onset of localized necking, are shown in Fig. 5a and b, respectively. Note that the digital grid is severely distorted in Fig. 5b (which was the final image recorded in this test), as it precisely followed the deformed shape of the tensile coupon. Once fracture occurred (shown in Fig. 5c), the correlation process was discontinued.

The displacements and strains were computed at each grid point. The spatial extent of the grid pattern and hence the region over which the calculation was conducted is user-controlled and therein lies one of the major advantages of the DIC technique over other methods. Unlike electromechanical strain gauges and extensometers, which do not provide measurement of localized deformation in the neck region of a tensile coupon (for example), and hence lead to the well-known drop in the stress–strain curve beyond diffuse necking, the DIC method offers direct user control of the area of the digital strain gauge used on each image. This enables accurate measurement of deformation and displacement fields within the neck region of a tensile coupon

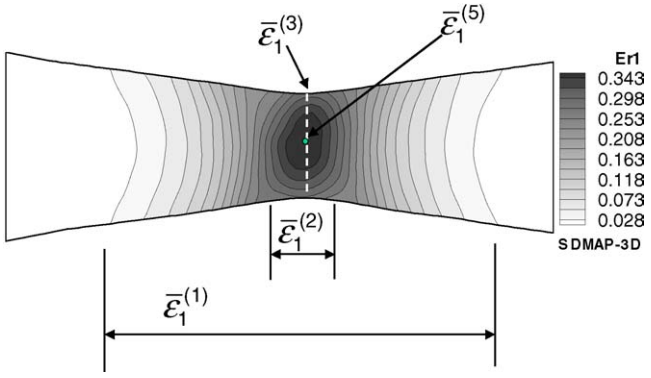

Fig. 6. Strain contour map of 2D axial strain field showing diffuse neck (red region) in a tensile coupon deforming in tension. Also shown are the 1D strain measures that are extracted from the corresponding 2D strain field.

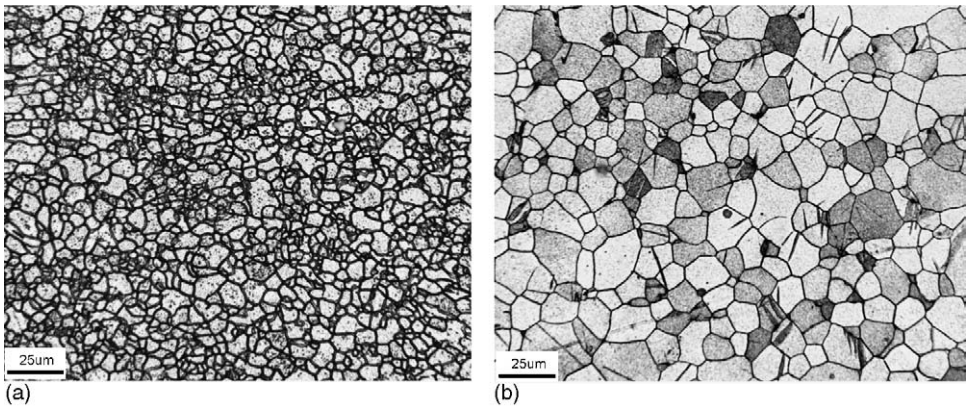

Fig. 7. Optical micrographs of two AZ31 alloys: (a) the base alloy (microstructure (1)) and (b) microstructure (2) after SHT at 450 °C for 10 min. Microstructure (3) (i.e. the aged alloy) is not shown due to its resemblance to microstructure (1).

(for example) and provides stress–strain curves that (typically) continue to increase beyond diffuse necking up to the point of localized necking. Such behavior is representative of the true tensile deformation behavior of the metal.

2.4. Extraction of true stress–strain curves from two-dimensional strain maps

The measured strain fields are represented by fringe patterns or maps, which are contours of constant strain levels. Fig. 6 shows a typical 2D map of a diffuse neck in the gauge section of a strained Mg tensile coupon. Individual (true) strain contour values are denoted by Er1 in the grayscale key to the right of the map. The maximum strain is near the center of the neck region (dark contours) and is 52.6%. Representative 1D (averaged) strain fields are computed from the measured 2D strains fields via the set of strain measures shown in Fig. 6 and described in greater detail in Appendix A [18].

Once strains at the tensile coupons surface are determined, the flow stress can then be calculated via the following force equilibrium equation:

$$\overline{\sigma}_1 \approx \frac{F}{WT} \exp(\overline{\varepsilon}_1) \quad (1)$$

where W and T are the initial width and thickness of the tensile coupon, $\overline{\varepsilon}_1$ is one of four average axial true strain measures in Appendix A, F the applied axial load, and $\overline{\sigma}_1$ is the average axial true stress, respectively. Once the average strain measures listed are computed, then the corresponding tensile stress is computed via Eq. (1).

3. Results and discussion

3.1. Magnesium alloy microstructures

Fig. 7a and b illustrates the two AZ31 microstructures that were heated for 1 and 10 min at 450 °C, respectively, i.e. microstructures (1) and (2). At the resolution of the optical microscope, the aged AZ31 microstructure (3) strongly resembled the base microstructure, and was therefore not included in Fig. 7. The microstructures in Fig. 7 appear as if they were single

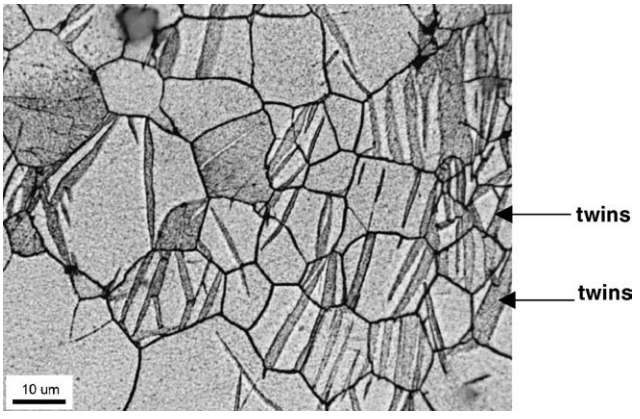

Fig. 8. Optical micrograph of the 10 min. SHT AZ31 (microstructure (2)) revealing the presence of twins.

phase, as expected from the solution heat-treatments (SHT), and also exhibited polygonal grain structures; however, their grain sizes were profoundly different. In microstructure (1) (heated for only 1 min at 450 °C), the average grain size measured using the linear intercept technique was 10 ± 2 μm, and varied from 4 μm to about 18 μm depending upon location. In

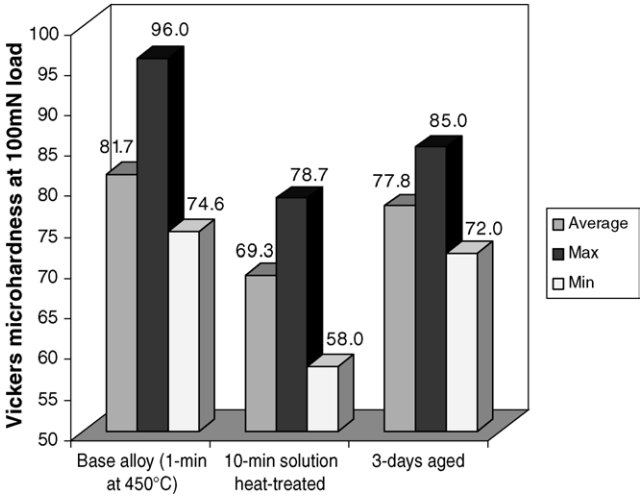

Fig. 9. Vickers microhardness test results comparing microstructures (1)–(3).

microstructure (2), the 10-min SHT grains ranged from 4 μm to over 50 μm, leading to an average grain size in the vicinity of 25 μm. In contrast with the base microstructure, the SHT microstructure with coarser grains also discolored after etching, a feature that strongly suggested preferential etching, and thus a dependence on crystallographic orientation. Over-etching microstructure (2) revealed twins that are shown at a higher magnification in Fig. 8. Twins, which are symmetrical intergrowths of adjacent crystals, appear as elongated microstructural features of differing lengths and widths with sizes that depend upon the grain size as well as other features (since a number of grains displayed no twins). They are typically intragranular and parallel to one-another. However, as noted in Fig. 8, some of the twins spread beyond grain boundaries. Some grains also appear more heavily twinned than others. Note that twinning was absent in both the microstructures (1) and (3). Although twins can result from polishing and/or strain accumulation (i.e. prior cold work), microstructure (2) was the only one of the three microstructures that exhibited twins both before and after tensile deformation.

The observation that twinning is only present in the coarse grain AZ31 microstructure (2) suggests that it may be the predominant plastic deformation mechanism in (2), while it will be less likely in the other alloys wherein thermally activated dislocation slip is a more favorable plastic deformation mechanism. This is consistent with work by Meyers et al. [26] suggesting that twin formation is suppressed by grain refinement and, in

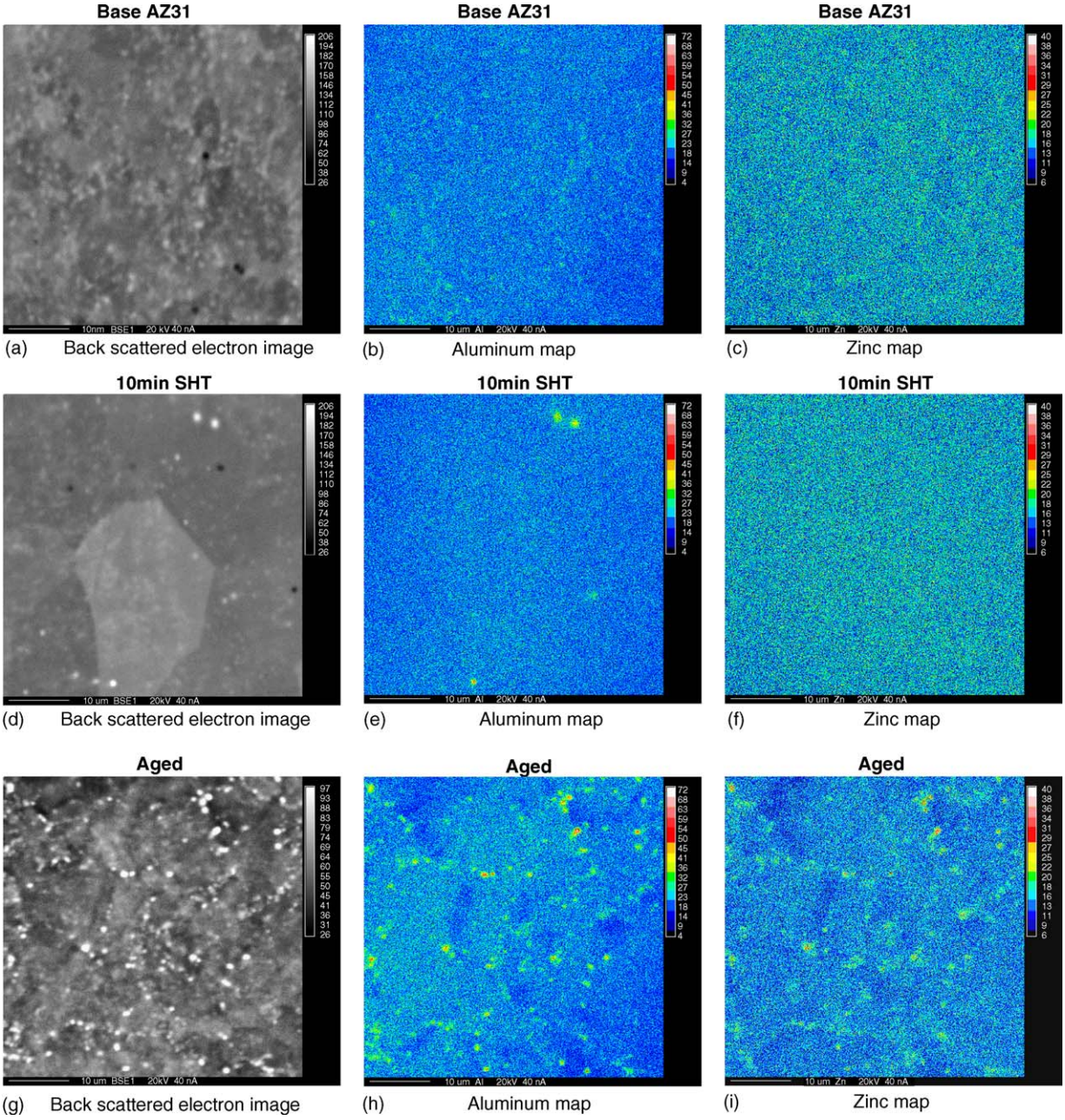

Fig. 10. Back-scattered electron images and compositional maps as measured with wavelength dispersive spectroscopy for the base (microstructure (1)), 10 min SHT (microstructure (2)), and aged (microstructure (3)) alloys.

Table 2
Selected X-ray diffraction angles with corresponding characteristics

Reflection ($h\,k\,l$)	2θ (°)	d-space (Å)	c (Å)	a (Å)	c/a	Kα peak (counts)
Mg phase (matrix)						
Base						
(1 0 3)	63.2442	1.46916	5.1981	3.1999	1.6244	604
(1 1 2)	68.8547	1.36249				122
Solution heat-treated						
(1 0 3)	63.2211	1.46964	5.1991	3.2020	1.6237	1080
(1 1 2)	68.8129	1.36322				182
Aged						
(1 0 3)	63.2187	1.46969	5.1998	3.2014	1.6242	711
(1 1 2)	68.8214	1.36307				220
$Mg_{17}Al_{12}$ phase						
Base						
(6 5 1)	70.2466	1.33887				34
Solution heat-treated						
(6 5 1)	70.1884	1.33983				44
Aged						
(6 5 1)	70.2000	1.33964				61

the case of pure Mg, by pyramidal $\{1\,0\,\bar{1}\,1\}\langle 1\,1\,\bar{2}\,0\rangle$ slip at temperatures above 225 °C [2]. It appears that the small grains of the base and aged microstructures prevented twinning in the deformation process.

Fig. 9 compares Vickers micro-hardness values for the three AZ31 microstructures, which are averages of indentation measurements at many locations. Note that the maximum and minimum hardness values are also indicated in Fig. 9. The hardness values for the base AZ31 microstructure (1) vary between 74.6 and 96 kg/mm^2: the average hardness is 81.7 kg/mm^2. The wide variation in hardness values can be explained (in part) in terms of the large grain size variation in this microstructure which is 4–18 μm (with a 10 μm average grain size). The SHT microstructure (2) had an average hardness of 69.3 kg/mm^2, which is about 15% less than that of the microstructure (1). The lower average hardness of the SHT microstructure (2) is consistent with its larger average grain size of 20 μm (and hence lower Hall–Petch strengthening) and also with its fully recovered state (10 min at 450 °C) compared to the base microstructure (1), which is not fully recovered because of the short SHT time (1 min at 450 °C). The maximum and the minimum hardness values, respectively, were 78.7 and 58 kg/mm^2, which indicate about as wide a spread in hardness values as observed in the base microstructure (1). Again wide variations in the hardness values were consistent with the wide range of grain sizes present in this microstructure. The aged microstructure (3) retained much of the hardness of the base microstructure (1), with a 77.8 kg/mm^2 average hardness compared to 81.7 kg/mm^2 for the base microstructure (1). This suggests that recovery during the low-temperature aging treatment was small and microstructure (3) was still noticeably work-hardened even after ageing. The range of hardness variations was narrower in microstructure (3), largely due to the lower maximum hardness value that was reduced from 96 kg/mm^2 in the base microstructure (1), to 85 kg/mm^2 in the aged microstructure (3). This decrease in the maximum hardness appears to be a consequence of elimination of some of the very fine grains from the base microstructure (1) as a result of the aging treatment. Whether the fine grain elimination during aging is due to grain growth or recrystallization remains unclear and requires further investigation. Partial recovery (i.e. reduction of pre-existing cold work) of the base microstructure (1) could be another reason for the slightly lower hardness maximum in the aged microstructure. The Vickers indentation technique also contributed to the large variations reported in Fig. 9 since the indenter tip was smaller than the average grain size of each microstructure. A smaller (and perhaps more representative) variation in hardness values is likely with a spherical indenter (e.g. in a Rockwell hardness test).

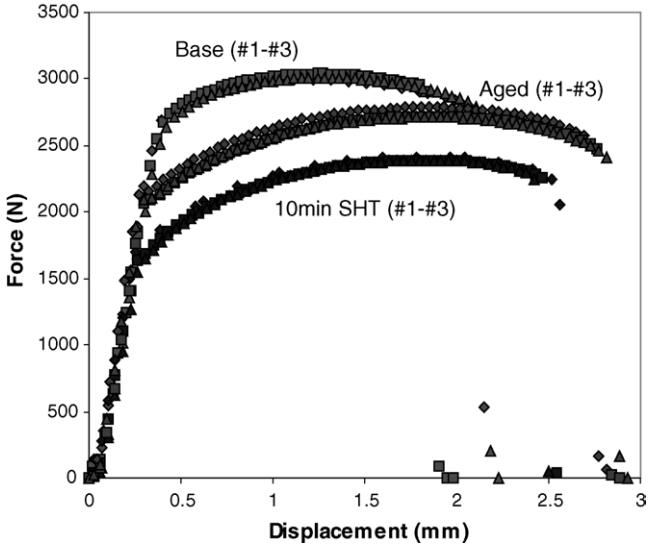

Fig. 11. Force–displacement curves derived from DASYLab [24] measurements.

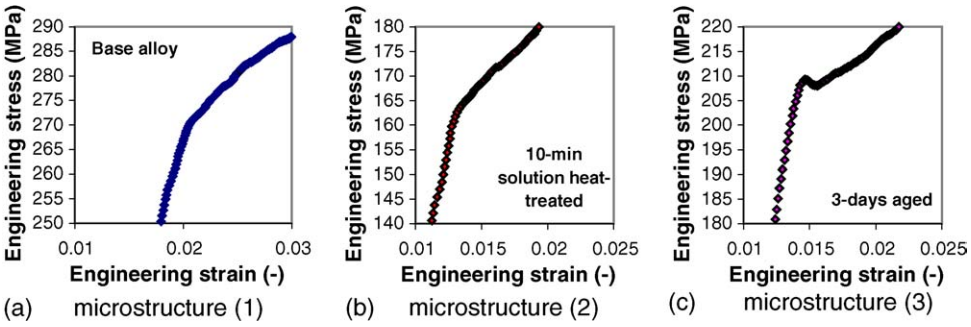

Fig. 12. Magnified views of the yield regions shown in Fig. 11.

Fig. 10 shows high-magnification compositional maps for the three AZ31 microstructures. The images in the left column show back-scattered images of each microstructure over an area of 50 μm × 50 μm. The images in the middle and right columns are X-ray intensity maps for Al and Zn, respectively. In the X-ray compositional maps, bright colors indicate regions of high concentration. The back-scattered images show the presence of a second phase in all three microstructures. However, as indicated by the optical micrographs in Fig. 7a and b, the base and 10-min SHT microstructures (1) and (2), respectively, are essentially single phase. In both of these microstructures, the alloying elements are fairly homogeneously distributed throughout. In the aged microstructure (3), precipitation of discreet particles at grain boundaries occurred, as expected from heat-treatment below the α-Mg solvus line. This phase is predominantly comprised of Al and Zn, and was identified as the equilibrium $Mg_{17}(Al,Zn)_{12}$ phase by X-ray diffraction.

Table 2 shows X-ray diffraction data for the three AZ31 microstructures. Only data from three high angle (2θ) peaks, with adequate resolution to differentiate between the microstructures, is shown. Of the three, two peaks belong to the α-Mg phase and one belongs to the $Mg_{17}(Al,Zn)_{12}$ phase. For the α-Mg phase, the lattice parameters of the hexagonal close pack cell, a and c, as well as the c/a ratio of the lattice cell are also shown. The 2θ, d, c and a values of the α-Mg phase in the 10-min SHT and the aged microstructures (2) and (3), respectively, are essentially identical. Similarly, all three c/a ratios are very close to that of pure Mg. These results strongly suggest that Al super saturation has little effect on the lattice spacing of the α-Mg phase. Relative to the solution-heat treated and the aged

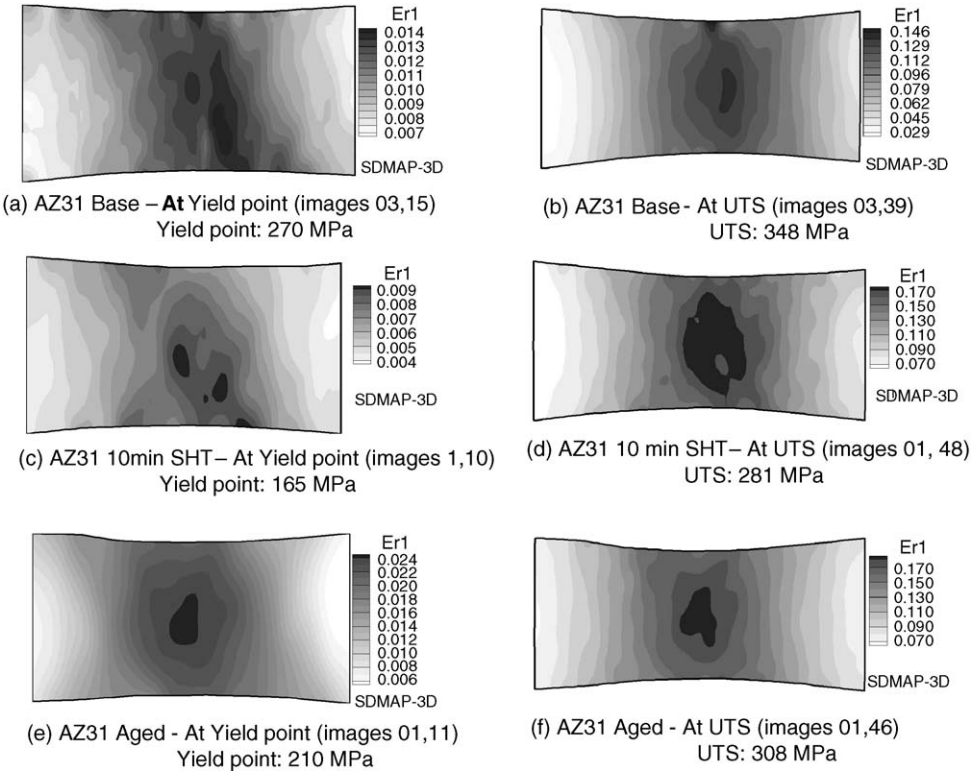

Fig. 13. Cumulative axial strain maps showing the neck region of each material at its yield point and ultimate tensile strength. The images that were compared are noted in each caption. Strain contours (Er1) could not be scaled to the same range due to the variation in peak strain values.

microstructures (2) and (3), respectively, the base microstructure (1) has slightly lower *d*, *c* and *a* values, which may be due to the work-hardened state of this essentially as-rolled material (one minute at 450 °C is not enough for full recovery). The Kα peak counts are highest for the 10-min SHT microstructure, which could be due either to the fully recovered state of this material or to texture changes associated with recrystallization during the SHT. The $Mg_{17}Al_{12}$ Kα-peak count is the highest in the aged microstructure (3), which is consistent with the highest precipitate concentration in this material.

3.2. Force–displacement curves

Fig. 11 shows raw force versus displacement curves acquired (via the DASYLab acquisition software) during tensile tests of nine Mg tensile coupons; i.e. three of each AZ31 microstructure. Tensile testing was repeated three times only, since the results were practically indistinguishable, as noted by the overlaying curves in Fig. 11. However, significant differences in the force–displacement responses are seen between the different microstructures. The yield points for the AZ31 base (1), 10-min SHT (2), and aged microstructures (3) are approximately 2700, 1500, and 2000 N, respectively. It is interesting to note that as strength decreased, displacement (and thus percent elongation) did not necessarily increase, as would be expected. In fact, the aged microstructure (3) exhibited the second highest strength level of all three materials and it was also the most ductile, with displacements approaching 3 mm (versus 2–2.5 mm for the other microstructures).

Fig. 12 shows magnified views of the yield regions in Fig. 11 in terms of the engineering stress versus engineering strain (generated by suitable normalization of the data of Fig. 11 over the initial cross-section area and the total gauge length of each test coupon) and shows the differences in yield characteristics of the microstructures investigated in this study. Note the yield point elongation in Fig. 12c (local maximum and minimum between 205 and 210 MPa) for the aged microstructure (3). This is an indication of a major change in the plastic deformation mechanism in this microstructure compared with the other two microstructures. The yield point behavior suggests an associated deformation mechanism involving solute/dislocation interactions or a precipitate effect, rather than twinning in the aged microstructure (recall that twins were observed only in microstructure (2)). Plastic deformation in the aged microstructure (3) beyond tensile strains associated with the yield point elongation most likely proceeds via dislocation slip.

3.3. Results from digital image correlation analysis

Fig. 13 shows cumulative strain maps for the axial component of strain (i.e. in the loading direction) for the three Mg microstructures. The errors in local in-plane displacements, rigid body rotation, and strain measurements were estimated to be 0.02 pixels, 0.02° and 100×10^{-6}, respectively, for a macroscopically homogenous field. Each contour pattern in Fig. 13 consists of levels with corresponding quantitative strain values denoted by Er1 in the associated legends. The images in the left column represent the axial strain state at the initial yield point as computed from the DIC analysis. The images in the right column represent the neck region in each microstructure at its corresponding ultimate tensile strength (UTS). Note that the tapering of these images is due to the change in the digital grid geometry as it followed plastic deformation of the coupon (this is best seen in Fig. 5b). Dark contours denote regions of high tensile strain, while gray–white contours denote regions of smaller tensile strains. Note that strain ranges for each material differ: this precludes a common scale for all maps. For example, the smallest peak strain of 0.9% occurs in the 10-min

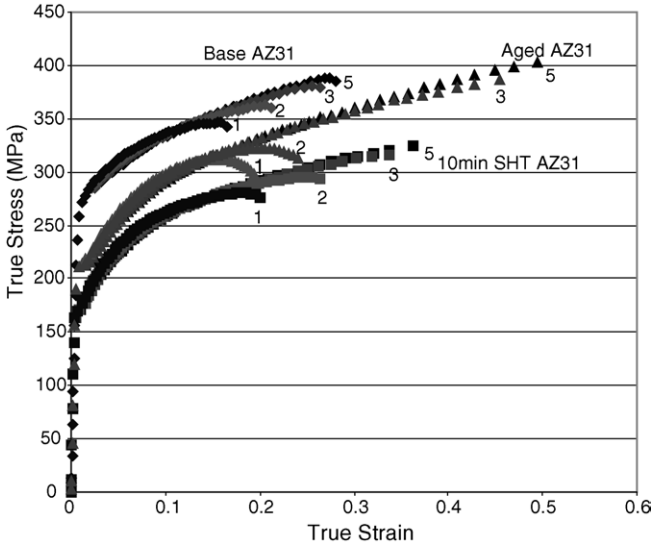

Fig. 14. Representative true stress–strain curves for the AZ31 base microstructure (1), 10 min SHT microstructure (2) and aged Mg microstructure (3) from the DIC analysis. Note that the number on each stress–strain curve designates one of the four the corresponding strain measures shown in Fig. 6 and given in Appendix A.

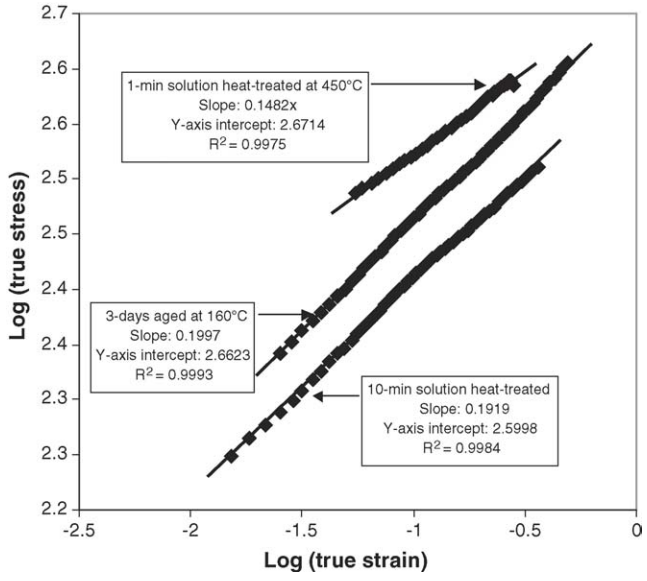

Fig. 15. Computed strain-hardening exponents for the three Mg microstructures using DIC-predicted true stress–true strain values.

SHT microstructure (2) (Fig. 13c). However, the largest peak strain at yield of 2.5% occurred in the AZ31 aged microstructure (3) (Fig. 13e). The strain contours corresponding to the diffuse neck region of the AZ31 aged microstructure (3) are the most uniform (see Fig. 13e) of the three strain maps in the left column in Fig. 13, while those corresponding to the 10-min SHT microstructure (2) are the least uniform. The yield points of the three materials are 270, 165, and 210 MPa, as listed in Fig. 13a, c and e, respectively. This is consistent with the force–displacement curves in Fig. 11. When each material achieves its UTS, the strain contour patterns in its neck region are more uniform, as seen in the figures in the right column in Fig. 13. The strain in each material is clearly larger at the UTS, with the AZ31 10-min SHT (2) and aged microstructures (3) accumulating the largest amount of strain (i.e. 17–18%). However, the 10-min SHT map showed the largest amount of material in the neck region at the 17–18% strain level. The UTS computed from the DIC analysis of the base (1), 10-min SHT (2), and aged (3) microstructures are 348, 281 and 308 MPa, respectively.

Fig. 14 shows the true stress–strain behavior of the base, 10-min SHT, and aged Mg microstructures, respectively, acquired via the DIC analysis. The significance of these plots over those in Figs. 11 and 12 is that they represent the behavior in the neck region of each microstructure beyond diffuse necking (which is essentially the limit of the "true" tensile behavior in Figs. 11 and 12). Note that the numbers 1–3 and 5 in Fig. 14 designate the four curves corresponding to the four different average strain measures listed in Appendix A. The most accurate representation of the true stress–strain behavior is the curve corresponding to Eq. (A3), which averages the 2D strain field along the narrowest width of the neck region in each tensile coupon [18]. Relative to this strain measure, the true stress of the base, 10-min SHT, and aged microstructures just prior to localized necking is 381, 318, and 385 MPa, respectively. A com-

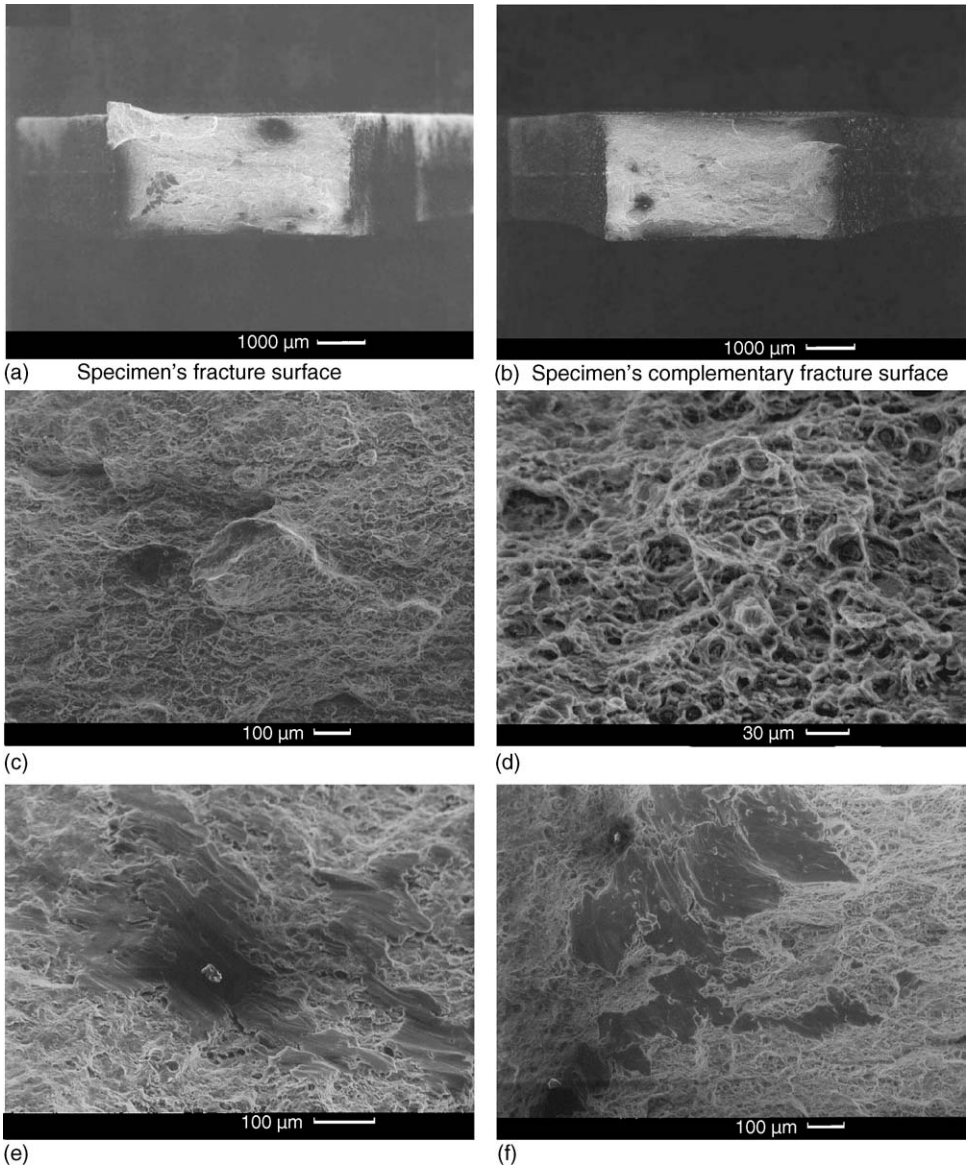

Fig. 16. SEM images of fracture surfaces of the AZ31 base microstructure (1).

parison of stress–strain curves in Fig. 14 suggests that the largest strains accumulated in the neck regions of the base, 10-min SHT, and aged microstructures were 25%, 34%, and 45%, respectively. Hence, the aged Mg microstructure (3) accumulates the largest amount of tensile strain prior to fracture, while the base microstructure (1) accumulates the least amount of strain prior to fracture. Note that the slight dip in each curve at the highest strain values results from the rapid thinning of the neck region just prior to fracture, and the inability of the image acquisition process to capture ample detail for the DIC analysis. This is in no way adversely affects the accuracy of the true stress–strain behavior at strain levels that precede fracture.

Selected true stress–true strain data from Fig. 14 (based on Eq. (A3)) were re-plotted in Fig. 15 using logarithmic scales to assess how well the data fit a simple power law equation $\sigma = K\varepsilon^n$ [27]. Data points at low plastic strains were left out of the plots. All three plots in Fig. 15 show excellent straight line fits through the data points, indicating that the true stress–true strain data for these alloys can be well represented by a simple power law. The slope of each line gives the work hardening exponent n of the material. As can be seen in Fig. 15, the work hardening exponents for the 10-min SHT microstructure (2) and aged microstructure (3) are very similar, although both microstructures have profoundly different grain sizes and their deformation mechanisms are likely very different (e.g. twinning versus dislocation slip). For these two microstructures, the work hardening exponent is about 0.19. For the base microstructure (1), the work hardening exponent is significantly less, i.e. about 0.15. The lower work hardening exponent of the base microstructure (1) is due to pre-existing cold work, which lowers the work hardening rate. The 10-min SHT and aged microstructures are apparently fully recovered and hence sustained an identical, high work hardening rate. A higher work hardening exponent pushes the maximum load point in a tensile test to a higher

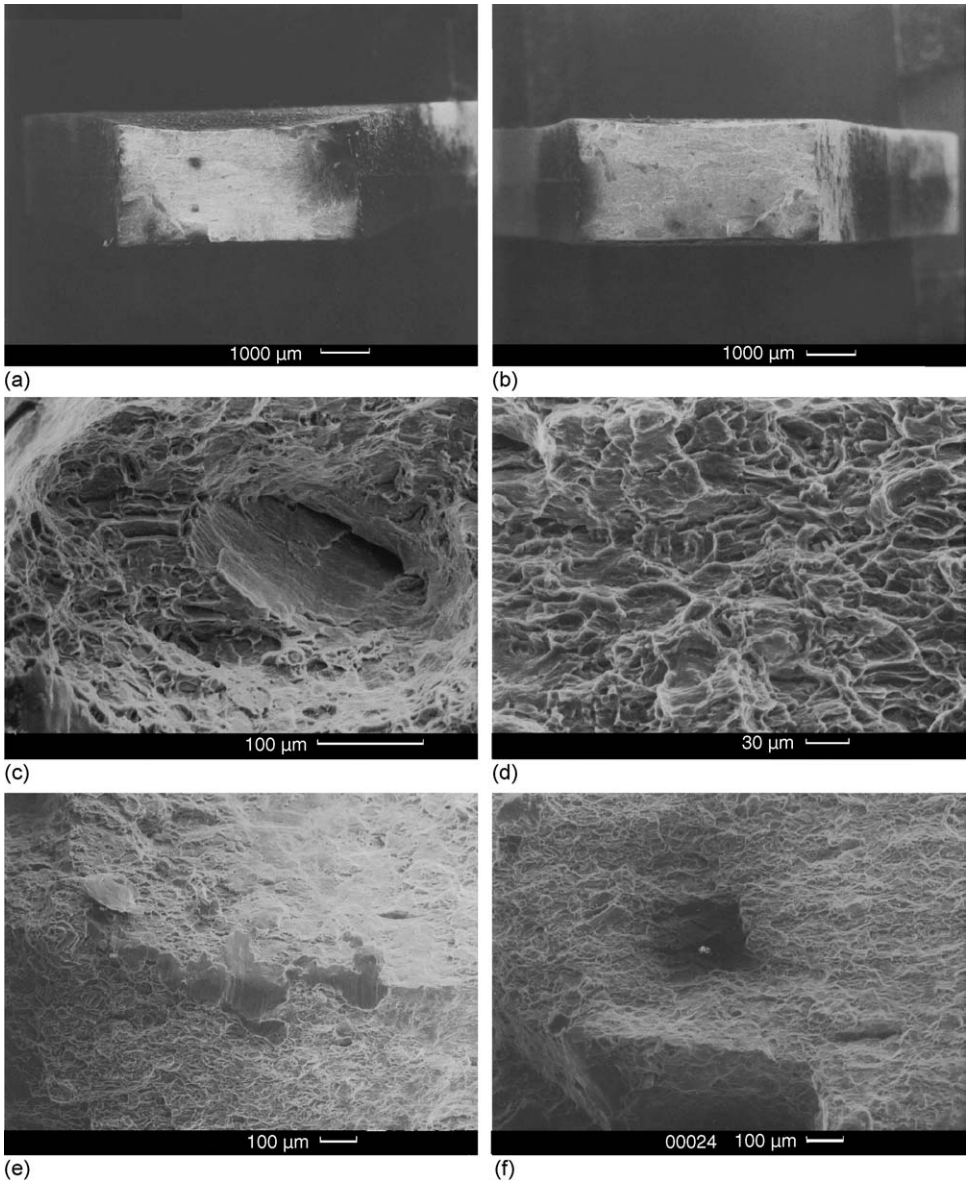

Fig. 17. SEM images of fracture surfaces of AZ31 10-min SHT microstructure (2).

strain level [28] giving higher uniform elongation values in the 10-min SHT and the aged microstructures. While the uniform elongation values of the 10-min SHT and the aged microstructures are essentially identical, the post-uniform elongation for the 10-min SHT microstructure (2) is smaller than that of the aged microstructure (3). As discussed earlier, these differences are due to different failure mechanisms associated with the large and the fine grain microstructures.

3.4. Fracture surfaces

Figs. 16–18 show secondary electron images of fracture surfaces of the base, 10-min SHT, and aged microstructures, respectively. The low-magnification images in Figs. 16 and 17a and b show dark regions in the fracture surfaces. High-magnification images of the dark regions, Figs. 16e and 17f, reveal the presence of a bright particle at the center of each dark region. The brightness of these particles is indicative of negative charge build accumulation. This suggests that these particles have a semi-metallic nature, and may in fact be oxides or intermetallic phases.

The high magnification images in Figs. 16 and 17d show brittle fracture by both inter-granular and trans-granular separation. The fracture morphology in Fig. 17d is coarser than in Fig. 16d, which is consistent with the larger grain size of the 10-min SHT microstructure (2) compared to the base microstructure (1). Plate-like features in Fig. 17c strongly suggest fracture either along twin boundaries or shear bands in this coarse grain alloy. In addition to the brittle fracture, all microstructures exhibited ductile fracture in the form of microvoids. High magnification images in Fig. 18 capture the morphology and the size distribution of microvoids in the fracture surface of the aged microstructure (3). Fig. 18e and f showed two distinctly different sizes of microvoids, i.e. large microvoids that were about 10–15

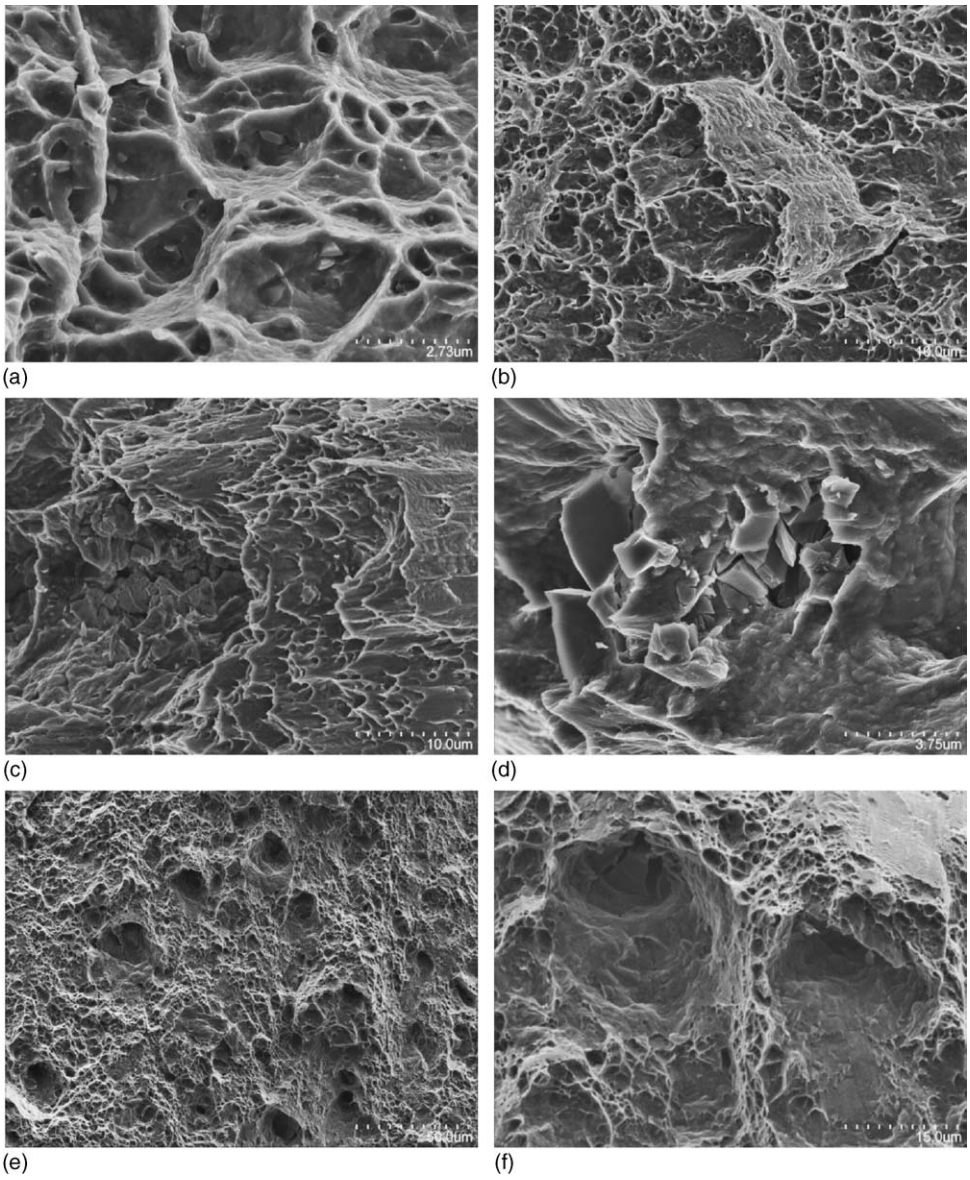

Fig. 18. SEM images of fracture surfaces of AZ31 aged microstructure (3).

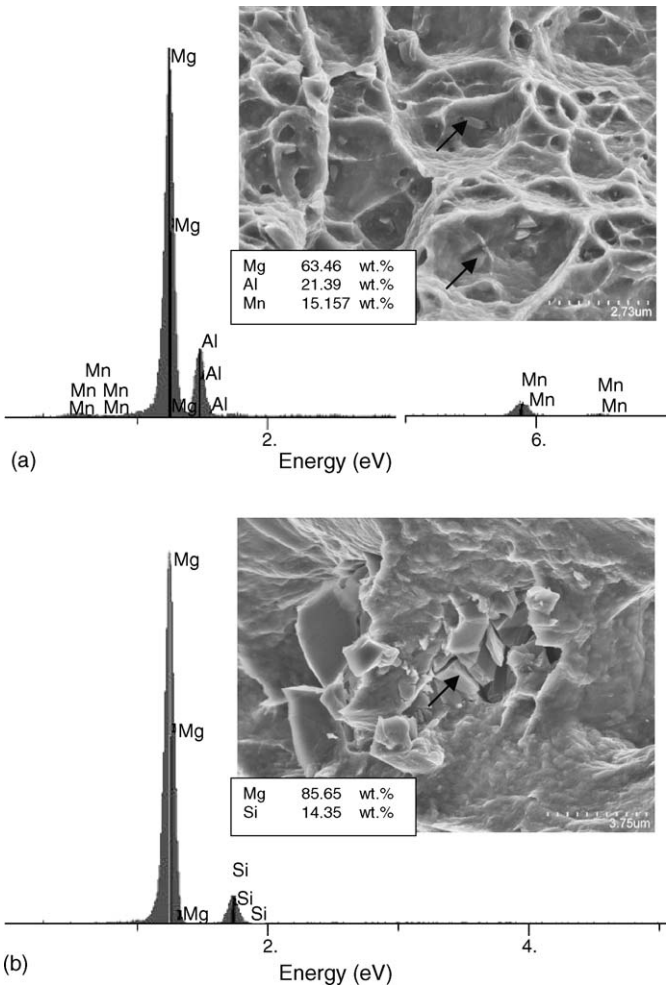

Fig. 19. Electron dispersive spectra and approximate chemical composition for second-phase particles found in the AZ31 aged microstructure (3).

times larger in diameter than smaller microvoids (1–2 μm). The size of large microvoids about matches the grain size in this microstructure, suggesting that the large microvoids are in fact grain pullouts in an otherwise ductile fracture. Fig. 18a and d shows close ups of the small and large microvoids, respectively, which reveal the presence of second phase particles inside. Electron dispersive spectroscopy (EDS) analysis of particles in the aged microstructure (3), shown in Fig. 19, suggests two distinct chemistries: sub-micron Mg–Al–Mn particles, and highly angular, glass-like particles, 1–2 μm size, based on Mg–Si. The composition of the Mg–Al–Mn phase in Fig. 19a is somewhat different from the expected second phase composition of $Mg_{17}(Al,Zn)_{12}$. There are two possible reasons for this difference: (a) the $Mg_{17}(Al,Zn)_{12}$ composition is based on the Mg–Al binary phase diagram and not on the Mg–Al–Mn ternary phase diagram, and (b) the EDS probe size is significantly larger than the micron to sub-micron size of the particles, and thus is prone to be biased towards the matrix composition i.e. Mg. The Mg–Si based particles were invariably found inside the large microvoids only, suggesting a strong association of the Si-based particles with the grain pull out/inter-granular fracture. The Mg–Si type particles were found in all three microstructures. These Si-based glass-like particles may have their origin in the slag residue, trapped in the microstructure during casting. How these particles affect the ductility of the alloys is not precisely known, but it is likely that they ultimately limit ductility. On the other hand, Mn particles in the aged microstructure (3) were precipitated by the aging treatment, and hence they were found in far smaller concentrations in the other microstructures. This suggests the possibility that Mn particles may in fact have enhanced the ductility of the aged microstructure (3) by some as yet unknown mechanism.

4. Conclusions

Tensile tests of three AZ31 Mg alloy microstructures, i.e. a single phase, fine equiaxed grain AZ31 (base) Mg microstructure (1); a single-phase coarse grain, 10-min SHT microstructure (2); a two-phase, fine equiaxed grain AZ31 Mg (aged) microstructure (3) (decorated with fine $Mg_{17}(Al,Zn)_{12}$ grain-boundary precipitates), were conducted to compare ductility and strength differences. The main goals of the work were to determine which of the three microstructures may have better room temperature formability (based upon uniaxial tensile tests) and what microstructural features may contribute to improved formability in conventional stamping processes. The digital image correlation technique was used to compute tensile stress–strain curves beyond diffuse necking for the three AZ31 microstructures, to investigate the uniformity of strain contours in the neck regions at the initial yield point and UTS, and to measure ductility via tensile elongation to failure. The DIC data was also employed to predict hardening rates of each microstructure using a simple power law. Raw tensile tests results revealed that the single phase, fine-grain AZ31 base microstructure (1) showed higher strength but lower ductility than the large-grain, 10-min SHT microstructure (2). The two-phase AZ31 aged microstructure (3), despite second-phase precipitation and finer grain size, exhibited lower strength compared to the base microstructure (1), but higher than the single-phase large-grain microstructure (2). However, the two-phase aged microstructure (3) exhibited the highest elongation of all three microstructures. These observations were confirmed quantitatively by the DIC analysis with predicted yields points of the base, 10-min SHT, and aged microstructures being 270, 165, and 210 MPa, respectively, and UTS values being 348, 281 and 308 MPa, respectively. The aged microstructure (3) accumulated the largest amount of strain in its neck region at the UTS compared with the other two microstructures. The largest strains that accumulated in the neck regions of the base, 10-min SHT, and aged microstructures were 28%, 34%, and 48%, respectively. The absence of twins in the aged microstructure (3) was reflected in its higher yield strength, and indicated that plastic deformation likely occurred initially via solute/dislocation interactions and then dislocation slip; this is a potentially useful condition for the delay of necking and increase in ductility. When compared with the fine grain AZ31 (base) microstructure (1), increased ductility of the aged microstructure (3) was attributed to a combination of the following factors: (1) cold-work recovery after prolonged exposure at low temperature, and (2) more uniform deformation (avoidance of shear

localization) due to the presence of fine $Mg_{17}(Al,Zn)_{12}$ precipitates. Fracture surface analyses revealed Mg–Si type particles in all three microstructures. These may result from slag residue trapped in the alloy during casting stage and could in fact limit ductility of each material.

In this study, the effects of recovery, grain size and the second phase could not be independently investigated. Future will involve a fourth AZ31 microstructure that combines large grain size with second phase particles, which, along with the results of the current study, will allow separation of the effects of grain size and second phases on tensile behavior of AZ31 Mg sheet alloys. Future work is to be directed at using high-speed digital photography to better quantity fracture events in AZ31 Mg alloys. A new high-speed digital camera (Phantom V9.0 from Vision Research) has been acquired for this purpose. This will provide a better estimate of fracture stresses/strains from the DIC technique.

Acknowledgments

The authors are grateful to Anita Weiner for the microhardness measurements, M. Balogh for the X-ray diffraction measurements, Greg Campeau for DASYLab and image programming. P.E. Krajewski and M.V. Verbrugge provide helpful commentary on an earlier version of the report.

Appendix A

In Eq. (1), the definition of the average axial true strain $\bar{\varepsilon}_1$ is somewhat flexible with the digital image correlation technique. Four definitions of the average axial true strain measures were employed in this study as shown in Fig. 6 (it is a typical cumulative axial strain map, just after the onset of diffuse necking in a tensile test). The corresponding mathematical definitions of the average strain measures are as follows:

$$\bar{\varepsilon}_1^{(1)} = \frac{1}{MN}\sum_{j=1}^{N}\sum_{i=1}^{M}\varepsilon_1(i,\, j), \tag{A1}$$

where $\bar{\varepsilon}_1^{(1)}$ is the axial strain averaged over the entire gage section (following the conventional tensile test methodology), M and N are the total numbers of grid points along the gage length and width directions, respectively, and $\varepsilon_1(i,j)$ is the local axial strain at each grid point (i, j) obtained via DIC:

$$\bar{\varepsilon}_1^{(2)} = \frac{1}{M_n N}\sum_{j=1}^{N}\sum_{i=M_1}^{M_1+M_n}\varepsilon_1(i,\, j), \tag{A2}$$

where $\bar{\varepsilon}_1^{(2)}$ is the axial strain averaged over the entire neck region (this is the lower bound estimate of average strain in the diffuse neck), M_1 and M_n are the starting and total number of grid points along the gage length direction of the neck region (see Fig. 6), respectively:

$$\bar{\varepsilon}_1^{(3)} = \frac{1}{N}\sum_{j=1}^{N}\varepsilon_1(M_0,\, j), \tag{A3}$$

where $\bar{\varepsilon}_1^{(3)}$ is the axial strain averaged along the bar cross-section with the smallest width (i.e. the neck center line at $i = M_0$, see Fig. 6):

$$\bar{\varepsilon}_1^{(5)} = \varepsilon_1(M_0, N_0) = \max_{j=1,N}[\varepsilon_1(M_0,\, j)], \tag{A4}$$

where $\bar{\varepsilon}_1^{(5)}$ is the maximum axial strain at the center of a diffuse neck corresponding to the grid point (M_0,N_0). This definition of axial strain provides the upper bound estimate of measurable average strain in the diffuse neck. Since the entire gage section was used to compute $\bar{\varepsilon}_1^{(1)}$, local strain heterogeneities and gradients were averaged-out over the gage section. Alternatively, the strain fields selected for computing $\bar{\varepsilon}_1^{(2)}$, $\bar{\varepsilon}_1^{(3)}$, and $\bar{\varepsilon}_1^{(5)}$, were measured over the entire neck region, or a selected part of the neck region, and hence local strain heterogeneities were more accurately quantified. Both analytical and numerical analyses have shown that the average axial true strains $\bar{\varepsilon}_1^{(2)}$ and $\bar{\varepsilon}_1^{(3)}$ as defined, respectively, by Eqs. (A2) and (A3), are the most accurate estimates [18] of *uniaxial* true strain and true stress (via Eq. (1)) beyond diffuse necking in various tensile bar geometries. The definitions $\bar{\varepsilon}_1^{(1)}$ and $\bar{\varepsilon}_1^{(5)}$ provide uniaxial true stress–strain curves that bound the actual uniaxial true stress–strain curve irrespective of tensile bar geometry.

References

[1] E.F. Emley, Principles of Magnesium Technology, Pergamon Press, London, 1966.
[2] C.S. Roberts, Magnesium and Its Alloys, John Wiley and Sons, New York, 1960.
[3] G.E. Totten, L. Xie, K. Funatani (Eds.), Handbook of Mechanical Alloy Design, Marcel Dekker, Inc., New York, 2004, pp. 487–538.
[4] J.B. Clark, Acta Metall. 16 (1968) 141–151.
[5] G. Song, A. Atrens, D.S. John, L. Zheng, in: K.U. Kainer (Ed.), Magnesium Alloys and Their Applications, Wiley–VCH, Munich, Germany (DGM, Weinheim), 2000.
[6] R. Schmid-Fetzer, J. Grobner, Adv. Eng. Mater. 3 (12) (2001) 947–961.
[7] Selection and Application of Magnesium and Magnesium Alloys, Metals Handbook, vol. 2, 10th ed., 1990, pp. 455–479.
[8] G.V. Raynor, The Physical Metallurgy of Magnesium and Its Alloys, Pergamon Press, New York, 1959.
[9] J.R. Morris, K.M. Ho, K.Y. Chen, G. Rengarajan, M.H. Yoo, Model. Simul. Mater. Sci. Eng. 8 (2000) 25–35.
[10] J. Enss, T. Everetz, T. Reier, P. Juchmann, in: K.U. Kainer (Ed.), Magnesium Alloys and Their Applications, Wiley–VCH, Munich, Germany (DGM, Weinheim), 2000.
[11] P. Krajewski, Elevated Temperature Forming of Sheet Magnesium Alloys, SAE Paper No. 2001-01-3104, Warrendale, PA, SAE, 2001.
[12] K. Siegert, S. Jaeger, in: Alan Luo (Ed.), Magnesium Technology, TMS, Warrendale, PA, 2004, pp. 87–90.
[13] J.H. Jackson, P.D. Frost, A.C. Loonam, L.W. Eastwood, C.H. Lorig, Trans. AIME 185 (1949) 149–168.
[14] R.S. Busk, D.L. Leman, J.J. Casey, Trans. AIME 188 (1950) 945–951.
[15] P.D. Frost, J.G. Kura, L.W. Eastwood, Trans. AIME 188 (1950) 1277–1282.
[16] J.G. Schroth, in: E.M. Taleff, P.A. Friedman, P.E. Krajewski, R.S. Mishra, J.G. Schroth (Eds.), Advances in Superplasticity and Superplastic Forming, TMS, 2004, pp. 9–20.
[17] J.L. Murray, Bull. Alloy Phase Diagrams 3 (1982) 60–74.
[18] W. Tong, H. Tao, X. Jiang, N. Zhang, M. Marya, L.G. Hector, X.Q. Gayden, Metall. Mater. Trans. 36A (2005) 2651–2669.
[19] W. Tong, H. Tao, N. Zhang, L.G. Hector, Scr. Mater. 53 (2005) 87–92.

[20] B.W. Smith, X. Li, W. Tong, Exp. Technol. 22 (4) (1998) 19–21.
[21] W. Tong, Exp. Technol. 28 (2004) 63–67.
[22] W. Tong, Exp. Mech. 44 (2004) 502–511.
[23] N. Zhang, W. Tong, Int. J. Plasticity 20 (2004) 523–542.
[24] http://www.dasylab.net/dasylab_english/.
[25] http://www.kammrath-weiss.com/english/about_us/unshome.htm.
[26] M.A. Meyers, O. Vohringer, V.A. Lubarda, Acta Mater. 49 (2001) 4025.
[27] G.E. Dieter, Mechanical Metallurgy, 3rd ed., McGraw-Hill, 1986.
[28] W.F. Hosford, R.M. Caddell, Metal Forming, Prentice-Hall, 1983, pp. 56–57.